CrossMark

Gap-opening Planets Make Dust Rings Wider

Jiaqing Bi (毕嘉擎)[1,2] ⬇, Min-Kai Lin (林明楷)[2,3] ⬇, and Ruobing Dong (董若冰)[1,4] ⬇

[1] Department of Physics and Astronomy, University of Victoria, Victoria, BC V8P 5C2, Canada; bijiaqing@uvic.ca, rbdong@uvic.ca
[2] Academia Sinica Institute of Astronomy and Astrophysics, Taipei 10617, Taiwan, Republic of China; mklin@asiaa.sinica.edu.tw
[3] Physics Division, National Center for Theoretical Sciences, Taipei 10617, Taiwan, Republic of China
[4] Kavli Institute for Astronomy and Astrophysics, Peking University, Beijing 100871, People's Republic of China

Abstract

As one of the most commonly observed disk substructures, dust rings from high-resolution disk surveys appear to have different radial widths. Recent observations on PDS 70 and AB Aur reveal not only planets in the disk, but also the accompanying wide dust rings. We use three-dimensional dust-and-gas disk simulations to study whether gap-opening planets are responsible for the large ring width in disk observations. We find that gap-opening planets can widen rings of dust trapped at the pressure bump via planetary perturbations, even with the midplane dust-to-gas ratio approaching order unity and with the dust back-reaction accounted for. We show that the planet-related widening effect of dust rings can be quantified using diffusion-advection theory, and we provide a generalized criterion for an equilibrated dust ring width in three-dimensional disk models. We also suggest that the ring width can be estimated using the gas turbulent viscosity α_{turb}, but with cautions about the Schmidt number being greater than order unity.

1. Introduction

Facilitating radio interferometers like the Atacama Large Millimeter/submillimeter Array (ALMA), many dust rings and gaps (e.g., HL Tau (ALMA Partnership et al. 2015) and TW Hya (Huang et al. 2018a)), as well as dust spirals (e.g., MWC 758 (Dong et al. 2018)) and lopsided dust clumps (e.g., IRS 48 (van der Marel et al. 2013)), have been revealed in protoplanetary disks (PPDs). Understanding the morphology of those detailed disk structures is critical to the topic of planet formation, as they could be the indicator of ongoing planet–disk interactions (Zhang et al. 2018; Hammer et al. 2021).

As one of the most commonly observed substructures (Andrews et al. 2018; Long et al. 2018; van der Marel et al. 2019), dust rings have different radial widths, with the ratio between the deconvolved full width at half maximum (FWHM) and the radius ranging from $\lesssim 10\%$ (e.g., AS 209 (Huang et al. 2018b)) to $\gtrsim 90\%$ (e.g., SR 24S (Cieza et al. 2021); see Figure 1). This wide range of widths indicates different relative strengths of dust trapping (e.g., gas drag in the pressure bump (Takeuchi & Lin 2002; Paardekooper & Mellema 2004) or traffic jams in the radial drift (Okuzumi et al. 2016; Jiang & Ormel 2021)) and dust diffusion (e.g., turbulence-induced diffusion (Youdin & Lithwick 2007)).

Gap-opening planets have now become a popular explanation for the formation of dust rings, because pressure bumps naturally arise from the gap-opening process (Lin & Papaloizou 1993). A great example of this scenario could be PDS 70, where two planets have been detected in the gap next to a dust ring (Keppler et al. 2018; Haffert et al. 2019; Benisty et al. 2021). In the meantime, this dust ring is visibly wider compared with many other well-resolved rings from disk surveys (see Figure 1). Similar things happen to AB Aur, where a planet is also detected next to a wide dust ring (Tang et al. 2017; Currie et al. 2022). We therefore question whether this large ring width is associated with planets, and how much, if associated, the planet can widen the dust ring.

To answer those, we perform three-dimensional grid-based hydrodynamic simulations of dusty PPDs with embedded gap-opening planets. We find that the planet can widen dust rings trapped at the pressure bump (see Figure 2). We also provide an analytical approach to estimate the dust ring width in such a scenario. Our results suggest that gap-opening planets could be a potential explanation for wide dust rings in PPDs.

This paper is organized as follows. We describe the disk–planet system of interest and different numerical models in Section 2. We present our results in Section 3, which includes three parts: The first part shows the widening effect of dust rings due to planet-related effects. The second part shows the combined effect of the planet and different levels of dust back-reaction on dust rings. The third part provides an analytical approach to estimate the dust ring width. In Section 4, we discuss the connection between dust diffusivity and gas turbulent viscosity under planet-related effects. Finally, we conclude in Section 5.

2. Planet–Disk Model

We consider a 3D protoplanetary disk composed of gas and dust with an embedded planet of mass M_{p} around a central star of mass $M_\star$. We neglect disk self-gravity, magnetic fields, planet orbital migration, and planet accretion. We use $\{r, \phi, \theta\}$ to denote spherical radius, azimuth, and polar angle, and $\{R, \phi, Z\}$ to denote cylindrical radius, azimuth, and height. Both coordinates are centered on the star.

In the following sections, the subscript "ref" denotes azimuthally averaged values at $R = R_{\mathrm{ref}}$ on the disk midplane, where R_{ref} is a reference radius. The subscript "0" is only used
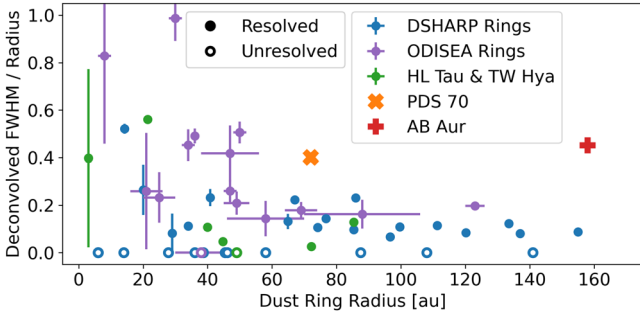
Figure 1. The ratio between the deconvolved full width at half maximum (FWHM) and the radius of observed dust rings. The deconvolution method can be found in Dullemond et al. (2018), with unresolved widths set to zero (open circles in the plot). Samples are selected from the DSHARP Program (Andrews et al. 2018; Huang et al. 2018b), the ODISEA Program (Cieza et al. 2021), HL Tau (ALMA Partnership et al. 2015), TW Hya (Huang et al. 2018a), PDS 70 (Benisty et al. 2021; Portilla-Revelo et al. 2022), and AB Aur (Tang et al. 2017). Rings without error bars in the DSHARP Program are not sampled.

for time-varying quantities, and it denotes their initial values. The symbol $\langle \rangle$ denotes azimuthally averaged values.

2.1. Basic Equations and Numerical Setups

Models in this paper use the same basic equations and numerical setups as those in Bi et al. (2021) (hereafter BLD21). Therefore, we only briefly list them here and refer readers to BLD21 for detailed descriptions and justifications.

The volumetric density, pressure, and velocity of gas are denoted by $\{\rho_g, P, V\}$. The time-independent, vertically isothermal, axisymmetric gas temperature and sound speed are given by $T(R) = T_{\rm ref}(R/R_{\rm ref})^{-q}$ and $c_s(R) = c_{s,\rm ref}(R/R_{\rm ref})^{-q/2}$. The isothermal equation of state and the pressure scale-height are given by $P = \rho_g c_s^2$ and $H_g = c_s/\Omega_K$, where $\Omega_K(R) = \sqrt{GM_\star/R^3}$ is the Keplerian angular velocity and G is the gravitational constant. The disk is assumed to be nonflared with a constant aspect ratio $h = H_g/R = 0.05$, corresponding to $q = 1$.

We consider a single species of dust modeled as a pressureless fluid with volumetric density and velocity $\{\rho_d, W\}$. The Epstein gas drag on the dust is parameterized by the Stokes number $\mathrm{St} = \tau_s \Omega_K$, where

$$\tau_s = \frac{\rho_{g,\rm norm}}{\rho_g} \frac{c_{s,\rm ref}}{c_s} \frac{\mathrm{St}_{0,\rm ref}}{\Omega_{K,\rm ref}} \qquad (1)$$

is the particle stopping time. $\rho_{g,\rm norm}$ is a normalization that equals to $\rho_{g0,\rm ref}$ in type A models (see Section 2.2).

The hydrodynamic equations for gas and dust are given by

$$\frac{\partial \rho_g}{\partial t} + \nabla \cdot (\rho_g V) = 0, \qquad (2)$$

$$\frac{\partial V}{\partial t} + V \cdot \nabla V = -\frac{1}{\rho_g}\nabla P - \nabla \Phi$$
$$+ \frac{\epsilon_\rho}{\tau_s}(W - V) + \frac{1}{\rho_g}\nabla \cdot \mathcal{T}, \qquad (3)$$

$$\frac{\partial \rho_d}{\partial t} + \nabla \cdot (\rho_d W) = 0, \qquad (4)$$

$$\frac{\partial W}{\partial t} + W \cdot \nabla W = -\nabla \Phi - \frac{1}{\tau_s}(W - V). \qquad (5)$$

Here, $\Phi = -GM_\star/r + \Phi_p + \Phi_{\rm ind}$ is the net gravitational potential composed of terms from the star, the planet, and the indirect planet–star gravitational interactions, respectively. The disk-related potential terms are neglected for the non-self-gravitating disk. $\epsilon_\rho = \rho_d/\rho_g$ is the *local* dust-to-gas ratio, which should be distinguished from the vertically integrated *global* dust-to-gas ratio $\epsilon_\Sigma = \Sigma_d/\Sigma_g$. $\mathcal{T}$ is the viscous stress tensor (see Equation (11) in BLD21), which involves a gas kinematic viscosity ν. We implement $\nu = 10^{-5}R_{\rm ref}^2\Omega_{K,\rm ref}$ to suppress interference such as vertical shear instability (Nelson et al. 2013) and vortex formation (Koller et al. 2003; Li et al. 2005, 2009; Lin & Papaloizou 2010) at gap edges. To isolate planet-related effects on the dust ring, turbulent-induced dust diffusion (Weber et al. 2019) is neglected. Unless otherwise specified, dust back-reaction on the gas is included.

We consider a planet on a fixed, circular orbit at $R = R_{\rm ref}$ on the disk midplane. The planet-related potential terms are

$$\Phi_p + \Phi_{\rm ind} = -\frac{Gm_p(t)}{\sqrt{r'^2 + r_s^2}} + \frac{Gm_p(t)}{R_{\rm ref}^2}R\cos(\phi - \phi_p), \quad (6)$$

where ϕ_p is the azimuth of the planet, $r_s = 0.1H_g$ is a smoothing length, and r' is the distance to the planet. Here, we define a time-dependent planet mass $m_p(t)$, with its value increasing gradually from zero to M_p (see Equation (14) in BLD21) at the start of simulations to avoid transient impacts of adding a full-mass planet to the disk. The planet's potential is turned on over a timescale of $t_g = 500T_{\rm ref}$, where $T_{\rm ref} = 2\pi\Omega_{K,\rm ref}^{-1}$ is the reference orbital period.

Our models are evolved by the FARGO3D code (Benítez-Llambay et al. 2016, 2019). We adopt a spherical domain centered on the star with $r \in [0.2, 4.0]R_{\rm ref}$, $\phi \in [0, 2\pi]$, and polar angle such that $\tan(\pi/2 - \theta) \in [-3h, 3h]$. The resolutions we choose are $N_r \times N_\theta \times N_\phi = 360 \times 90 \times 720$, with logarithmic spacing in r and uniform spacing in θ and ϕ.

The gas density is damped to its initial value at radial boundaries, and is assumed to be in vertical hydrostatic equilibrium at vertical boundaries. The dust density is symmetric at both radial and vertical boundaries. The meridional velocities of gas and dust are set to zero at radial and vertical boundaries, except that the inner radial boundary is open for mass loss of dust. The azimuthal velocities at those boundaries are assigned at the Keplerian speed with a pressure offset for gas. Periodic boundaries are imposed in the ϕ direction.

2.2. Models

The models in our paper are categorized into three types, namely type A, B, and C. The three types differ in the prescription of gas evolution and initial conditions. In type A models, the initial radial profile of dust surface density Σ_{d0} is a power-law function, whereas in type B and C models, Σ_{d0} is a Gaussian radial bump. Different from that in type B models, the evolution of $\{\rho_g, V\}$ is artificially stalled in C, which means they are time-invariant.
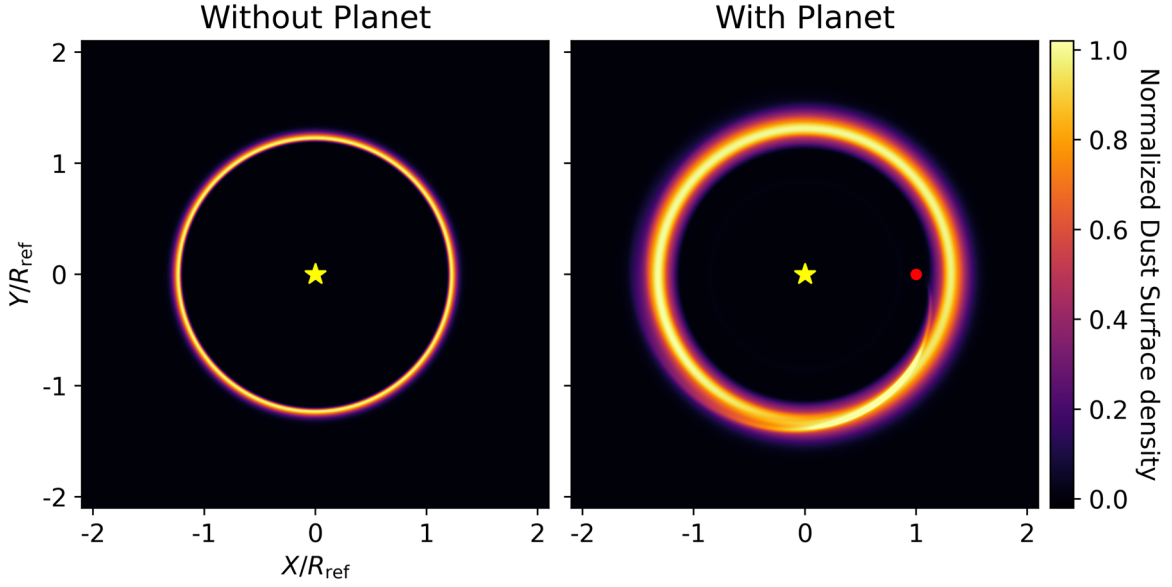
Figure 2. The face-on view of dust rings trapped at the pressure bump. The left panel shows a dust ring in a disk model with no planet (Model C1), and the right panel shows a dust ring in the disk with a Saturn-mass gap-opening planet (Model C5; see Sections 2.2 and 3.1 for descriptions and applications). Both snapshots are taken at $t = 1000T_{\rm ref}$ in each model and are normalized individually by the radial peak in the azimuthally averaged profile. The radial profiles of dust surface density are shown in Figure 3. The yellow star indicates the location of the central star and the red dot indicates the location of the planet.

2.2.1. Type A Models: How Will M_p and St Affect the Widening Effect?

Type A models are used to *quantitatively* study how planet-related effects would change the radial width of dust rings at the outer gap edge. The corresponding results are shown in Sections 3.3 and 4. There are 12 type A models with different planet masses $M_{\rm p}$ ranging from $2 \times 10^{-4}M_\star$ to $7 \times 10^{-4}M_\star$, and two initial reference Stokes numbers $St_{0,\rm ref} = 10^{-3}$ and 10^{-2}. Here, we define the model with $\{M_{\rm p}, St_{0,\rm ref}\} = \{3 \times 10^{-4}M_\star, 10^{-3}\}$ as the fiducial model, representing a Saturn-mass planet around a solar-mass star, with 0.1 mm sized grains at ~ 45 au in a young PPD such as HL Tau.[5]

The initialization of gas and dust in type A models are the same as those in BLD21. The axisymmetric gas density profile is initialized to

$$\rho_{\rm g0} = \rho_{\rm g0,ref}\left(\frac{R}{R_{\rm ref}}\right)^{-p} \times \exp\left[\frac{GM_\star}{c_{\rm s}^2}\left(\frac{1}{r} - \frac{1}{R}\right)\right], \qquad (7)$$

with $p = 1.5$ and $\rho_{\rm g0,ref}$ being arbitrary for a non-self-gravitating disk. The dust density is initialized to

$$\rho_{\rm d0} = (\epsilon_{\rho 0}\rho_{\rm g0})|_{Z=0} \times \exp\left(-\frac{Z^2}{2H_\epsilon^2}\right), \qquad (8)$$

where $\epsilon_{\rho 0}|_{Z=0} = 0.1$ and $H_\epsilon = H_{\rm g}H_{\rm d}(H_{\rm g}^2 - H_{\rm d}^2)^{-1/2}$ is valued such that the dust scale-height $H_{\rm d0} = 0.1H_{\rm g}$ and $\epsilon_{\Sigma 0} = 0.01$. The azimuthal velocities are initialized to

$$V_{\phi 0} = R\Omega_{\rm K}\left(\sqrt{1 - 2\eta} + \frac{\epsilon_{\rho 0}\eta}{\epsilon_{\rho 0} + 1}\frac{1}{St'^2 + 1}\right) \qquad (9)$$

$$W_{\phi 0} = \sqrt{\frac{GM_\star}{r}} - R\Omega_{\rm K}\left(\frac{\eta}{\epsilon_{\rho 0} + 1}\frac{1}{St'^2 + 1}\right), \qquad (10)$$

where $St' = St/(1 + \epsilon_\rho)$, and $2\eta = (p + q)h^2 + q(1 - R/r)$ is a dimensionless measurement of the radial pressure gradient. The radial velocities are initialized to

$$V_{R0} = \frac{2\epsilon_{\rho 0}\eta}{\epsilon_{\rho 0} + 1}\frac{St'}{St'^2 + 1}R\Omega_{\rm K} \qquad (11)$$

$$W_{R0} = -\frac{2\eta}{\epsilon_{\rho 0} + 1}\frac{St'}{St'^2 + 1}R\Omega_{\rm K}. \qquad (12)$$

And the initial vertical velocities are $V_{Z0} = W_{Z0} = 0$.

2.2.2. Type B Models: How Will Dust Back-reaction Affect the Widening Effect?

Type B models are used to *qualitatively* study the effect of different levels of dust back-reaction on the dust ring width. The corresponding results are shown in Section 3.2 and Figure 4. The models include a gas gap already opened by a planet, as well as a Gaussian dust ring at the outer gap edge. There are five type B models, namely B1 to B5, with different levels of dust load in the dust ring.

To have a gas gap opened by the planet, the gas initialization $\{\rho_{\rm g0}, \boldsymbol{V}_0\}$ in all type B models are taken from the snapshot at $t = 3000T_{\rm ref}$ in the fiducial type A model (i.e., $\{M_{\rm p}, St_{0,\rm ref}\} = \{3 \times 10^{-4}M_\star, 10^{-3}\}$), in which the gap profile has almost reached an equilibrium state. Here, we set $t_{\rm g} = 0$ to maintain the initial gap profile, and consequently, the planet mass is fixed at $m_{\rm p} = 3 \times 10^{-4}M_\star$.

Dust grains in type B models have $St_{0,\rm ref} = 10^{-3}$. The dust density is initialized to an axisymmetric Gaussian ring with

$$\rho_{\rm d0} = \frac{\Sigma_{\rm d0}}{\sqrt{2\pi}H_{\rm d0}} \times \exp\left[-\frac{(R - R_{\rm pmax})^2}{2w_{\rm d0}^2} - \frac{Z^2}{2H_\epsilon^2}\right], \quad (13)$$

where $H_{\rm d0} = 0.1H_{\rm g}$, $R_{\rm pmax} = 1.243R_{\rm ref}$ is the radius of the midplane pressure maximum, and $w_{\rm d0} = H_{\rm g,ref}$ is the initial radial width of the ring. $\Sigma_{\rm d0}$ is valued such that $\epsilon_{\Sigma 0} = \{5 \times 10^{-4}, \ 5 \times 10^{-3}, \ 5 \times 10^{-2}, \ 5 \times 10^{-1}, \ 5\}$ at

---

[5] Here, we assume that the grain internal density is 1.5 g cm^{-3}, the total disk mass is 0.2 $M_\odot$ (Booth & Ilee 2020), the outer disk radius is 150 au, and the surface density power-law index is -1.5.

Table 1
Dust Load Initialization of Type B Models

Model	$\epsilon_{\Sigma 0}^{\max}$
B1	0.0005
B2	0.005
B3	0.05
B4	0.5
B5	5

Note. $\epsilon_{\Sigma 0}^{\max}$ is the initial dust-to-gas surface density ratio at the radial peak of the dust ring. Except for the dust load, all the other dust and gas initial conditions are identical for all type B models.

$R = R_{\mathrm{pmax}}$ in Model B1, B2, B3, B4, B5, respectively (see Table 1). We note that $\epsilon_{\Sigma 0}$ for Model B3 best reproduces the dust load level of the ring at $t = 3000T_{\mathrm{ref}}$ in the fiducial type A model. The dust velocities in all type B models are initialized to $W_{\phi 0} = \sqrt{GM_\star / r}$ and $W_{R0} = W_{Z0} = 0$.

2.2.3. Type C Models: Isolating the Multiple Effects Caused by the Planet

Type C models are used to *qualitatively* study how various planet-related effects would change the dust ring width. The corresponding results are shown in Section 3.1 and Figure 3. Like type B models, these models also include a Gaussian dust ring and a gas gap, but the further evolution of gas density and velocity is stalled to control variables.

There are five type C models to isolate planet-related effects, which are differentiated by the initialization of gas and whether planetary potential terms are included (see Table 2). The face-on views of gas initialization in Model C1 and C5 are provided in Appendix A to visualize the differences. The initialization of dust in all type C models is identical to that in Model B3 (i.e., an axisymmetric Gaussian ring with $\epsilon_{\Sigma 0} = 0.05$ at $R = R_{\mathrm{pmax}}$ and $\mathrm{St}_{0,\mathrm{ref}} = 10^{-3}$). In Model C1, the prescription of the planet is identical to the one in type B models. To avoid errors while disabling gas evolution, the gas damping effect at boundaries and dust back-reaction on the gas are disabled as well.

3. Results

3.1. Dust Rings Widened by the Gap-opening Planet

Compared with pressure bumps that are not planet-related (e.g., formed at the edge of dead zones or condensation frontiers), those at the outer edge of planet-opened gaps are additionally perturbed, as they are periodically swept by planetary wakes. In the meantime, dust grains trapped in those pressure bumps feel the wakes in two ways: perturbations in the gas density field that change the local stopping time of dust, and perturbations in the gas velocity field that change the velocity of dust. Here, we show that these two mechanisms, together with the insignificant nonaxisymmetric planetary potential on the dust (see below), can widen the dust ring.

Figure 3 shows the dust surface density profile in type C models at $t = 1000T_{\mathrm{ref}}$. We first focus on the comparison between Model C1 and C5 in the top panel, which are static-gas models including a Gaussian dust ring at the edge of a planet-opened gap, with all three planet-related effects preserved in Model C1 and eliminated in C5 (see Table 2). Starting from the same initialization, the dust ring in Model C1 becomes much wider, whereas that in C5 continues to
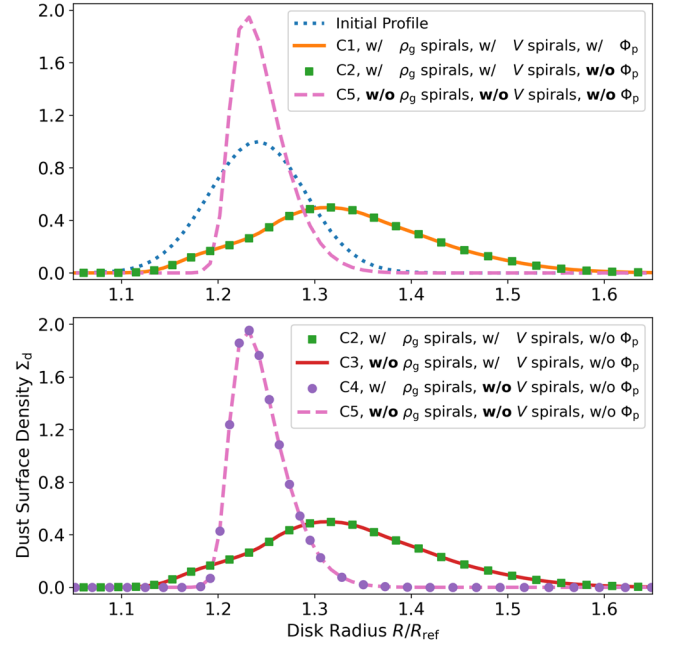

Figure 3. The azimuthally averaged dust surface density at $t = 1000T_{\mathrm{ref}}$ in type C models. Two panels are provided for more convenient comparisons. All profiles are normalized to the peak value in the initial profile. The initial profile peaks at the radius of the pressure maximum in the midplane. The corresponding face-on views in Model C1 and C5 are provided in Figure 2.

concentrate to the pressure maximum. This comparison shows that the net effect of the three planet-related effects widens the dust ring.

We then question which effect of the three contributes the most to the widening effect. We isolate the three effects by turning off the planetary potential and individually modifying ρ_g and V in Models C2, C3, and C4 (see Table 2), respectively. In the top panel of Figure 3, the comparison between Models C1 and C2 shows that the planetary potential on the dust is insignificant. In the bottom panel, {C2 versus C3} and {C4 versus C5} show that the perturbation in the gas density field is not the dominant effect. Finally, {C2 versus C4} and {C3 versus C5} show that it is the planetary wakes in the gas velocity field that are most responsible for the widening of the dust ring.

Meanwhile, we note that the dominance of gas velocity perturbations may only be applicable to the well-coupled dust ($\tau_s \ll \Omega_K^{-1}$) in our models, for which the terminal velocity approximation (Youdin & Goodman 2005; Jacquet et al. 2011; Price & Laibe 2015; Lovascio & Paardekooper 2019)

$$W = V + \frac{\nabla P}{\rho_g (1 + \epsilon_\rho)} \tau_s \qquad (14)$$

is always dominated by the gas kinematics term, even if the density perturbations launched by the planet can lead to changes of τ_s by a few tens of percent. For larger grains in the disk, we would expect the density perturbations to play a more important role. Besides, we note that dust rings in Models C1, C2, and C3 are carried to larger radii while being widened by planet-related effects. This is the result of disabling dust back-reaction, which is required by the no-gas-evolution implementation and will be discussed in Section 3.2.

Table 2
Gas Initialization of Type C Models

Model	ρ_g	V_R	V_ϕ	V_Z	$\Phi_p + \Phi_{ind}$	Axisymmetry
C1	ρ'_g	V'_R	V'_ϕ	V'_Z	Included	with density spirals
						with velocity spirals
C2	ρ'_g	V'_R	V'_ϕ	V'_Z	Neglected	with density spirals
						with velocity spirals
C3	$\langle\rho'_g\rangle$	V'_R	V'_ϕ	V'_Z	Neglected	without density spirals
						with velocity spirals
C4	ρ'_g	0	$\sqrt{R^2\Omega_K^2\left(1 - \frac{3}{2}\frac{Z^2}{R^2}\right) + \frac{R}{\rho'_g}\frac{\partial P'}{\partial R}}$	0	Neglected	with density spirals
						without velocity spirals
C5	$\langle\rho'_g\rangle$	0	$\sqrt{R^2\Omega_K^2\left(1 - \frac{3}{2}\frac{Z^2}{R^2}\right) + \frac{R}{\langle\rho'_g\rangle}\frac{\partial \langle P'\rangle}{\partial R}}$	0	Neglected	without density spirals
						without velocity spirals

Note. The superscript "'" in this table denotes evaluations from the snapshot at $t = 3000T_{ref}$ in the fiducial Type A model, which are asymmetric fields with planet-driven spirals and meridional flows. The symbol $\langle\rangle$ denotes azimuthally averaged values. The values of V_ϕ in models C4 and C5 assume hydrodynamic equilibrium. All values listed in this table are time-invariant in type C models. The last column explains the outcome of modifying $\{\rho_g, \boldsymbol{V}\}$ fields. The velocity spiral refers primarily to the nonzero gas radial velocity correlated to the planet-driven spirals.

3.2. The Effect of Dust Back-reaction on Dust Rings

For a long time, numerical disk models neglected dust back-reaction on the gas for simplicity and to reduce computational cost. This approximation worked well because conventional notions indicate a low dust-to-gas ratio ($\epsilon_\rho \ll 1$) in proto-planetary disks. However, Kanagawa et al. (2018) showed that in dust rings, where the dust concentrates, effective dust back-reaction is capable of flattening the radial profile of the pressure bump, leading to a broadened dust ring. Therefore, dust back-reaction is critical to the study of dust ring morphology.

To show that a gap-opening planet can widen dust rings on top of the effect of dust back-reaction, we make comparisons among type B models, which also include a Gaussian dust ring and a gas gap, but with different dust load levels. Different from the type C models in Section 3.1, the type B models here include the gas evolution and dust back-reaction. The top panel of Figure 4 shows how different levels of dust back-reaction would change the dust ring morphology on top of the same planet-related effects.

First, we find that in Models B1 and B2, in which dust back-reaction is negligible due to low dust load, the dust rings are widened and moved outward as much as that in Model C1. Then, in Models B3 and B4, in which the midplane dust-to-gas ratio is close to one, the rings become narrower compared with those in Models B1 and B2, and are closer to the pressure maximum.

The comparison between models of low and moderate dust load levels confirms that dust back-reaction helps dust to resist effects that are related to the gas kinematics. When the dust back-reaction is negligible (Model B1 and B2) or even neglected (Model C1), the planetary wakes are capable not only of widening the dust ring but also providing an outward net mass flux that, together with the gas meridional flows, carries well-coupled dust grains outward. When the dust back-reaction is moderately strong ($\epsilon_\rho \sim 1$), the dust ring can still be widened, albeit to a lesser extent, and it becomes harder for it to be carried outward by gas flows, as it acts like a damper to those effects.

Therefore, we conclude that when ϵ_ρ increases from 0 to 1, the dust ring at the edge of the planet-opened gap would become narrower. It may seem to contradict the result in Kanagawa et al. (2018), which states effective dust back-reaction would flatten the global pressure profile and make the dust ring wider, but it does not. In Models B3 and B4, the maximum *local* density ratio ϵ_ρ^{max} is close to one, but the vertically integrated *global* surface density ratio ϵ_Σ^{max}, which is the term monitored in the 2D disk model in Kanagawa et al. (2018), is much smaller. This means even though the dust can deform the pressure profile close to the midplane via back-reaction, the gas on top of the midplane can compensate for that. Similar phenomena can be seen from the comparison between the axisymmetric (radial-vertical), unstratified disk models in Taki et al. (2016) and the stratified models in Onishi & Sekiya (2017). In our models, this argument is supported by the bottom panel of Figure 4, which shows that the gas density profiles from Models B1 to B4 are all consistent with each other. When it comes to both $\epsilon_\Sigma^{max} > 1$ and $\epsilon_\rho^{max} > 1$ in Model B5, the dust ring becomes so dust-rich that it is capable of deforming the global gas density profile via overwhelming back-reaction. Then the dust ring becomes wider as a result of the pressure profile being flattened, in agreement with Kanagawa et al. (2018).

To conclude, moderate dust back-reaction ($\epsilon_\rho \sim 1$) tends to make the dust ring narrower by damping the planetary perturbations. However, when $\epsilon_\Sigma > 1$ and $\epsilon_\rho > 1$, the ring expands itself during the process of deforming the global pressure profile via overwhelming back-reaction, with the widening effect being no more attributable to the planet-related effects. We note that Model B3 provides the most similar dust load level to our type A models ($\epsilon_\rho^{max} \sim 0.5$) in Section 3.3 and conventional models of protoplanetary disks. Therefore, the dust rings in our type A models tend to demonstrate the minimum width under the net effect of planetary perturbations and dust back-reaction.

3.3. How Much Can the Dust Ring Be Widened by a Planet?

The radial FWHM of an equilibrated dust ring w_d is determined by the balance between the concentration effect due to pressure gradient and the expansion effect due to diffusion. Therefore, in our models without the turbulence-induced dust
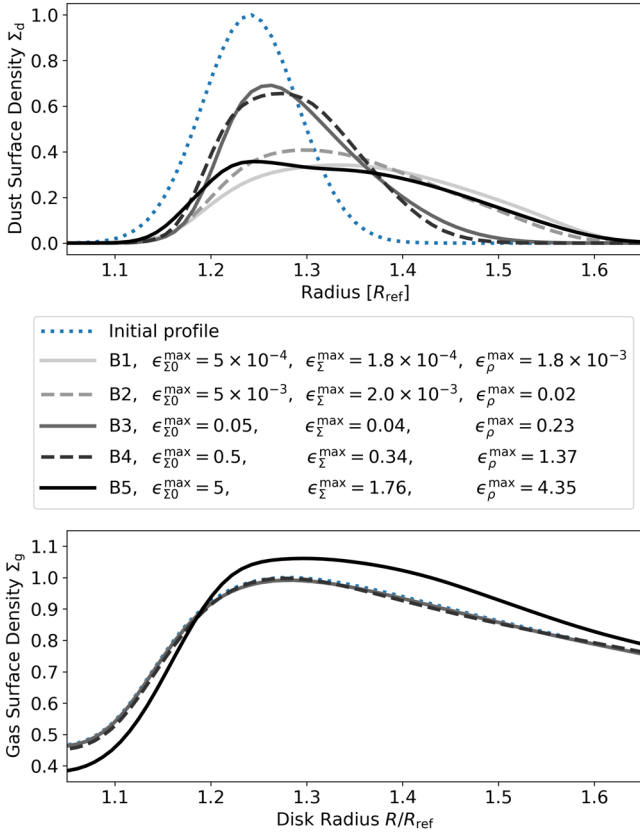
Figure 4. The azimuthally averaged dust surface density (top) and gas surface density (bottom) at $t = 1000T_{\rm ref}$ in type B models. All profiles are normalized to the corresponding maximum value in the initial profile. Because dust rings in different models are initialized with the same radial width but different dust load levels, we only compare the radial location and width of profiles in the top panel. The maximum values of the dust-to-gas surface density ratio $\epsilon_\Sigma^{\rm max}$, as well as its initial value $\epsilon_{\Sigma 0}^{\rm max}$ and the corresponding midplane density ratio $\epsilon_\rho^{\rm max}$, are listed in the legends.

diffusion, if the planet can widen dust rings and maintain this effect, the dust rings can be modeled as being widened by an effective diffusion with a diffusion tensor $\mathcal{D}$. In this section, we first try to establish a quantification of $\mathcal{D}$ via gradient diffusion hypothesis, and then derive the relation between $\mathcal{D}$ and $w_{\rm d}$.

3.3.1. Quantify $\mathcal{D}$ with Gradient Diffusion Hypothesis

The planet-related effects expand dust rings via introducing fluctuations to the disk, which may be modeled as diffusion. If so, we would like to quantify those fluctuations in order to obtain the diffusion coefficients. In our disk models, a physical variable A can be azimuthally decomposed to $A = \langle A \rangle + \Delta A$, where $\langle A \rangle$ is the mean field and ΔA is the fluctuation term with $\langle \Delta A \rangle = 0$. Applying the decomposition to Equation (3) and then taking the azimuthal average, we get

$$\frac{\partial \langle \rho_{\rm d} \rangle}{\partial t} = -\nabla \cdot (\langle \rho_{\rm d} \rangle \langle \boldsymbol{W} \rangle) - \nabla \cdot \langle \Delta \rho_{\rm d} \Delta \boldsymbol{W} \rangle. \quad (15)$$

The product term of fluctuations above is associated with diffusion via the gradient diffusion hypothesis (e.g., Cuzzi et al. 1993; Tominaga & Takahashi 2019):

$$\langle \Delta \rho_{\rm d} \Delta \boldsymbol{W} \rangle = -\mathcal{D} \nabla \langle \rho_{\rm d} \rangle, \quad (16)$$

where

$$\mathcal{D} = \begin{bmatrix} \mathcal{D}_{RR} & \mathcal{D}_{RZ} \\ \mathcal{D}_{ZR} & \mathcal{D}_{ZZ} \end{bmatrix} \quad (17)$$

is a diffusion tensor that describes the dust diffusion in the frame of the disk. We note that only diffusions in the $\{R, Z\}$ directions are considered here, as the ϕ components become irrelevant in Equation (15). Equation (16) provides a quantification of $\mathcal{D}$, but it does not give a unique solution, because it only has two equations for the four components of $\mathcal{D}$. Therefore, we assume $\mathcal{D}_{RZ} = \mathcal{D}_{ZR} = 0$, indicating the radial gradient of density does not contribute to vertical diffusion, and vice versa, to reduce number of unknowns. Then, for conciseness, we use $\mathcal{D}_R$ and $\mathcal{D}_Z$ to denote $\mathcal{D}_{RR}$ and $\mathcal{D}_{ZZ}$, respectively. Nevertheless, $\mathcal{D}$ at the dust peak (where $\nabla \langle \rho_{\rm d} \rangle = 0$), which is the key for the widening effect of the dust ring, cannot be quantified via Equation (16). Therefore, we quantify $\mathcal{D}$ via balancing the advection term and the diffusion term in Equation (15), in a steady state where $\partial \langle \rho_{\rm d} \rangle / \partial t = 0$. Later, in Section 3.3.3, we will show that a profile of $\mathcal{D}$ with $\nabla \mathcal{D} \sim 0$ in the extent of the dust ring, and a scenario where advection and diffusion are balanced in individual directions, are preferred while associating $\mathcal{D}$ with $w_{\rm d}$. Therefore, here we would expect a constant $\overline{\mathcal{D}}$ at the dust ring with

$$\nabla_Z \cdot (\langle \rho_{\rm d} \rangle \langle W_Z \rangle) = \overline{\mathcal{D}}_Z \nabla_Z^2 \langle \rho_{\rm d} \rangle \quad (18)$$

$$\nabla_R \cdot (\langle \rho_{\rm d} \rangle \langle W_R \rangle) = \overline{\mathcal{D}}_R \nabla_R^2 \langle \rho_{\rm d} \rangle. \quad (19)$$

We then run type A models to validate this method. Different from those in type B and C models, gas and dust densities in type A models are both initialized to power-law radial profiles, with no gaps or rings. When simulations begin, the planet mass increases from zero and gradually opens a gap, which eventually leads to the formation of a dust ring. Type A models are differentiated by the planet mass and Stokes number, with the model of $\{M_{\rm p}, {\rm St}_{0,{\rm ref}}\} = \{3 \times 10^{-4} M_\star, 10^{-3}\}$ being the fiducial one. To provide near-steady states, all type A models are run for $3000T_{\rm ref}$.

The profiles of terms in Equations (18) and (19), evaluated vertically and radially across the dust peak, are shown in panels (a) and (b) of Figure 5. We choose constant values of $\overline{\mathcal{D}}$ and find no good match between the advection term and the diffusion term. Panel (a) shows that, while the vertical profile of the diffusion term is an even function relative to the midplane, the profile of the advection term is close to an odd one. In our model, this qualitative mismatch is resulted from a meridional flow that not only crosses the midplane but also penetrates through the dust layer, which breaks the symmetry along the midplane that is conventionally assumed in previous studies. The meridional flows affect the radial profiles as well. In panel (b), although the two profiles are similar in a large radial extent, they have different zero-crossings, indicating negative diffusion coefficient in part of the ring. Besides, the two profiles diverge at $R \sim 1.23 R_{\rm ref}$, which is still within the half width at half maximum to the peak. In addition, we note that the two mismatches in the radial and vertical direction do not compensate for each other, and they cannot be fixed by setting nonzero values of $\overline{\mathcal{D}}_{RZ}$ and $\overline{\mathcal{D}}_{ZR}$ (see Appendix B). Therefore, we conclude that this method of quantifying a constant $\overline{\mathcal{D}}$ at the dust ring using the gradient diffusion hypothesis is not applicable to our disk models with active meridional flows induced by gap-opening planets.
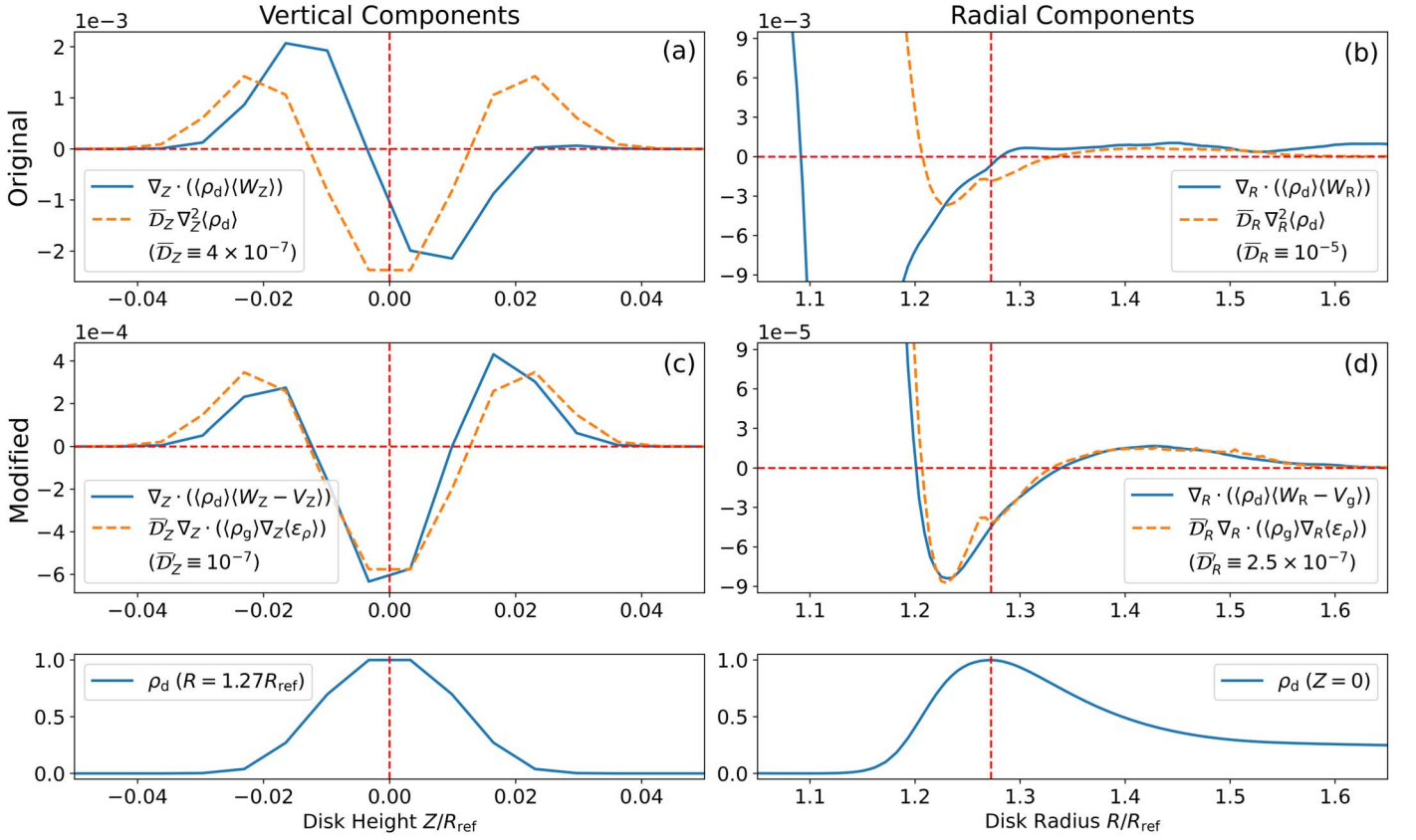
Figure 5. (a): The vertical profile of terms in Equation (18) at the dust peak. (b): The radial profile of terms in Equation (19) in the midplane. (c): The vertical profile of vertical components in Equation (23) at the dust peak. (d): The radial profile of radial components in Equation (23) in the midplane. All profiles are evaluated in the fiducial type A model at $t = 3000 T_{\rm ref}$. The demonstrative constant diffusion coefficients $\overline{\mathcal{D}}$ and $\overline{\mathcal{D}}'$, in the unit of $R_{\rm ref}^2 \Omega_{\rm K,ref}$, are chosen such that the two curves in each panel are at the same order of magnitude. Panels (a) and (b) represent the original gradient diffusion hypothesis in Section 3.3.1. Panels (c) and (d) represent the modified gradient diffusion hypothesis in Section 3.3.2. Panels (a) and (c) are normalized to the midplane dust density at the dust peak. Panels (b) and (d) are normalized to the radial profile of the midplane dust density. The vertical red dashed lines in the left column denote $Z = 0$, while the ones in the right column denote the dust peak at $R = 1.27 R_{\rm ref}$. The horizontal red dashed lines denote $y = 0$. The normalized vertical and radial profiles of dust density are shown in the bottom for reference.

3.3.2. Modifying the Gradient Diffusion Hypothesis

In our models, the advection of well-coupled dust is correlated to the gas kinematics. However, the method in the above section does not have any explicit dependence on the gas. Here, we show that, after taking the nontrivial gas density and velocity field into consideration, a *modified* gradient diffusion hypothesis can model fluctuations of the relative motion between gas and dust.

To address the effects of bulk motion and fluctuation of gas, we first apply the azimuthal decomposition to Equation (2) to get

$$\frac{\partial \langle \rho_{\rm g} \rangle}{\partial t} = -\nabla \cdot (\langle \rho_{\rm g} \rangle \langle \boldsymbol{V} \rangle) - \nabla \cdot \langle \Delta \rho_{\rm g} \Delta \boldsymbol{V} \rangle. \qquad (20)$$

Considering both fluctuation terms in Equations (15) and (20), we modify Equation (16) (to be justified a posteriori) to

$$\begin{aligned} \nabla \cdot \langle \Delta_{\rho_{\rm d}} \Delta \boldsymbol{W} \rangle &- \langle \epsilon_\rho \rangle \nabla \cdot \langle \Delta_{\rho_{\rm g}} \Delta \boldsymbol{V} \rangle \\ &= -\nabla \cdot (\mathcal{D}' \langle \rho_{\rm g} \rangle \nabla \langle \epsilon_\rho \rangle), \end{aligned} \qquad (21)$$

where $\langle \epsilon_\rho \rangle = \langle \rho_{\rm d} \rangle / \langle \rho_{\rm g} \rangle$ is the mean field dust-to-gas ratio. Here, $\mathcal{D}'$ is the diffusion tensor that describes the diffusion of dust *relative to* the gas, also with nondiagonal elements assumed to be zero. Instead of the steady state for both gas and dust with $\partial \langle \rho_{\rm d} \rangle / \partial t = \partial \langle \rho_{\rm g} \rangle / \partial t = 0$, we suggest that $\mathcal{D}'$ can be

quantified in a more general case with

$$\frac{D \langle \epsilon_\rho \rangle}{Dt} = \frac{\partial \langle \epsilon_\rho \rangle}{\partial t} + \langle \boldsymbol{V} \rangle \cdot \nabla \langle \epsilon_\rho \rangle = 0. \qquad (22)$$

Equation (22) is an advection equation that says the Lagrangian derivative of $\langle \epsilon_\rho \rangle$ is zero. That is, the dust-to-gas ratio following a gas parcel remains constant. Considering Equations (15), (20), and (21), Equation (22) is equivalent to (see Appendix C)

$$\nabla \cdot (\langle \rho_{\rm d} \rangle \langle \boldsymbol{W} - \boldsymbol{V} \rangle) + \nabla \cdot (\mathcal{D}' \langle \rho_{\rm g} \rangle \nabla \langle \epsilon_\rho \rangle) = 0, \qquad (23)$$

which says the relative advection between gas and dust balances the relative diffusion between them.

We note that the dust and gas in the above state are not necessarily steady ($\partial / \partial t \neq 0$). For example, Equations (22) and (23) are still applicable when the dust and gas are moving together in space due to bulk motions while maintaining no relative evolution. In other words, for the purpose of associating $\mathcal{D}'$ with $w_{\rm d}$ in Section 3.3.3, we only need an equilibrated $w_{\rm d}$. We also note that the combination of Equations (22) and (23) agrees with the correct[6] advection–diffusion equation in the context of protoplanetary disks discussed in Desch et al. (2017).

---

[6] Other forms may lead to inappropriate derivations with wrong coefficients or unphysical terms.

Figure 5 (panels (c) and (d)) shows the profiles of terms in Equation (23). We find that the relative diffusion and advection balance in both directions, and the match of profiles can be obtained by constant $\overline{\mathcal{D}}'_R$ and $\overline{\mathcal{D}}'_Z$, but with different values. Therefore, we conclude that the radial component of diffusion coefficient $\mathcal{D}'_R$ at the dust peak can be quantified using the modified gradient diffusion hypothesis, and it can be approximated as a constant value in the radial extent of the dust ring.

3.3.3. Associating $\mathcal{D}'$ with the Dust Ring Width w_d

After quantifying $\mathcal{D}'_R$, the dust ring width w_d can be obtained with certain dust and gas density profiles. For simplicity, in this section we focus on the correlation between $\mathcal{D}'_R$ and w_d within the immediate vicinity of the dust peak in the midplane. For conciseness, all variables in this section are azimuthally averaged by default. Although ρ_d and ρ_g may not peak at the same location, we assume $\partial \rho_g / \partial R \sim 0$, and consequently $\partial \epsilon / \partial R \sim 0$, in the vicinity.[7]

As we show in Figure 5, the balance in Equation (23) can be reached in individual directions. Here, we write the radial part of it:

$$-\frac{\partial}{\partial R}[R\rho_d(W_R - V_R)] + \frac{\partial}{\partial R}\left(R\mathcal{D}'_R\rho_g \frac{\partial \epsilon_\rho}{\partial R}\right) = 0. \quad (24)$$

With the dust kinematics in our models agreeing with the terminal velocity approximation (Equation (14)), after rewriting $\rho_g \partial \epsilon_\rho / \partial R = \partial \rho_d / \partial R - \epsilon_\rho \partial \rho_g / \partial R$, and considering the locally isothermal equation of state and the power-law radial temperature profile, we get

$$\frac{\partial}{\partial R}\left[\epsilon_\rho R\left(\frac{\tau_s c_s^2}{1 + \epsilon_\rho} + \mathcal{D}'_R\right)\frac{\partial \rho_g}{\partial R}\right.$$
$$\left. - \epsilon_\rho q R \frac{\tau_s c_s^2}{1 + \epsilon_\rho} \frac{\rho_g}{R} - R\mathcal{D}'_R \frac{\partial \rho_d}{\partial R}\right] = 0. \quad (25)$$

Assuming $\partial \mathcal{D}'_R / \partial R \sim 0$ in the vicinity,[8] and recalling previous assumptions of $\partial \rho_d / \partial R \sim \partial \rho_g / \partial R \sim \partial \epsilon_\rho / \partial R \sim 0$ there, the terms with first-order derivatives in Equation (25) can be dropped, and Equation (25) can be approximated to

$$\epsilon_\rho\left(\frac{\tau_s c_s^2}{1 + \epsilon_\rho} + \mathcal{D}'_R\right)\frac{\partial^2 \rho_g}{\partial R^2} + \frac{q^2}{2}\frac{\tau_s c_s^2}{1 + \epsilon_\rho}\frac{\rho_d}{R} - \mathcal{D}'_R \frac{\partial^2 \rho_d}{\partial R^2} = 0. \quad (26)$$

To associate Equation (26) with the radial width of disk structures, we assume both gas and dust density profiles in the vicinity are Gaussian:

$$\rho_g(R) = \rho_g(R_g) \times \exp\left[-\frac{(R - R_g)^2}{2w_g^2}\right] \quad (27)$$

$$\rho_d(R) = \rho_d(R_d) \times \exp\left[-\frac{(R - R_d)^2}{2w_d^2}\right]. \quad (28)$$

---

[7] This approximation is appropriate in our type A models with moderate ($\epsilon_\rho \sim 1$) dust back-reaction.
[8] This approximation is discussed in Section 3.3.2.

R_g and R_d are the radii where the gas and dust density profile peak, and w_g and w_d are the widths of the dust ring and the gas bump. By approximating $w_g^2 \gg (R - R_g)^2$ within the vicinity of the dust peak, we find

$$\frac{\partial^2 \rho_g}{\partial R^2} = \rho_g \frac{(R - R_g)^2 - w_g^2}{w_g^4} \approx -\frac{\rho_g}{w_g^2} \quad (29)$$

$$\frac{\partial^2 \rho_d}{\partial R^2} = \rho_d \frac{(R - R_d)^2 - w_d^2}{w_d^4} \approx -\frac{\rho_d}{w_d^2}. \quad (30)$$

Then taking those back to Equation (26), we finally get

$$w_d = \sqrt{\frac{\mathcal{D}'_R}{\left(\frac{\tau_s c_s^2}{1 + \epsilon_\rho} + \mathcal{D}'_R\right)\frac{1}{w_g^2} - \frac{\tau_s c_s^2}{1 + \epsilon_\rho}\frac{q^2}{2R^2}}}, \quad (31)$$

which shows how much the dust ring can be widened by the diffusion-like behavior, given the radial location, the stopping time, the dust-to-gas ratio, the sound speed profile, and the gas structure at the dust ring. We note that, in the limit of $w_g^2 \ll 2R^2/q^2$ and $(1 + \epsilon_\rho)\mathcal{D}'_R \ll \tau_s c_s^2$, Equation (31) can be approximated to

$$w_d = w_g \sqrt{\frac{(1 + \epsilon_\rho)\mathcal{D}'_R}{\tau_s c_s^2}}, \quad (32)$$

which is similar to Equation (46) in Dullemond et al. (2018), but with different definitions of parameters.

4. Discussion

4.1. Connection to the Turbulent Viscosity

In this paper, we provide a way to associate the planet-related diffusion coefficient $\mathcal{D}'_R$ with the dust ring width w_d. However, in disk observations, $\mathcal{D}'_R$ is neither measurable nor a property that can be easily constrained by measurables, making it hard to infer any properties of the suspected planet using the dust ring width. Here, we discuss the feasibility of associating $\mathcal{D}'_R$ of the dust component with the Reynolds stress $\mathcal{R}$ of the gas component, which describes the radial turbulent angular momentum transport in the disk and is more easily constrained in observations.

In our 3D disk model, we calculate the azimuthally averaged profile of the Reynolds stress via

$$\mathcal{R} = \langle \rho_g \Delta V_R \Delta V_\phi \rangle, \quad (33)$$

where ΔV is the fluctuation of gas velocity to its mean field. Then the turbulent viscosity parameter α_{turb} (Shakura & Sunyaev 1973) can be obtained via

$$\alpha_{turb} = \mathcal{R}/\langle P \rangle = \frac{\nu_{turb}}{c_s H}, \quad (34)$$

where ν_{turb} is the measured kinematics viscosity and may not be identical to the implemented ν in the model. Because the ratio between the momentum diffusivity (i.e., the kinematics viscosity) and the mass diffusivity (i.e., the diffusion coefficient) is the Schmidt number Sc, Equations (31) and (32) can be rewritten to

$$w_d = \left[\left(1 + \frac{1}{\psi^2}\right)\frac{1}{w_g^2} - \frac{1}{\psi^2}\frac{q^2}{2R^2}\right]^{-1/2} \quad (35)$$
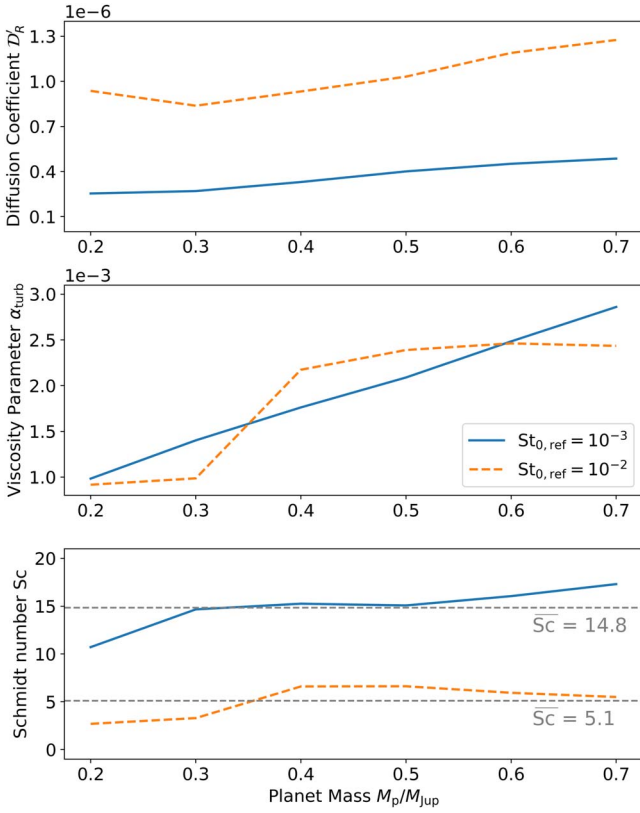
Figure 6. The radial diffusion coefficient $\mathcal{D}'_R$ (top) from Equation (24), the turbulent viscosity parameter α_{turb} (middle) from Equation (34), and the corresponding Schmidt number Sc (bottom) at the dust peak in different type A models. All profiles are evaluated in the midplane at $t = 3000 T_{\text{ref}}$. The unit of $\mathcal{D}'_R$ in the top panel is $R^2_{\text{ref}} \Omega_{\text{K,ref}}$. Horizontal dashed lines in the bottom panel mark the averaged Schmidt number $\overline{\text{Sc}}$ for models with the same $\text{St}_{0,\text{ref}}$.

and

$$w_{\text{d}} = w_{\text{g}} \psi, \tag{36}$$

where

$$\psi = \sqrt{\frac{(1 + \epsilon_\rho) \mathcal{D}'_R}{\tau_{\text{s}} c_{\text{s}}^2}} = \sqrt{\frac{(1 + \epsilon_\rho) \alpha_{\text{turb}}}{\text{St Sc}}}. \tag{37}$$

Figure 6 shows the measured $\mathcal{D}'_R$, α_{turb}, and the corresponding Schmidt number at the dust peak in type A models with different planet masses and Stokes numbers of dust. Our resulted α_{turb} values agree with the accretion levels estimated in disks with one or more planets of a few Earth masses in previous works (Goodman & Rafikov 2001; Fung & Chiang 2017). In the meantime, we show that the resulted Schmidt number is larger than the conventionally assumed of order unity. These large Sc numbers suggest that the planet-related transport of mass and momentum may depend on the specific form of turbulence or perturbation. Therefore, we advise caution with regard to the assumption of $\text{Sc} = 1$ in studies on turbulent effects in protoplanetary disks. For models with the same $\text{St}_{0,\text{ref}}$, we find the Schmidt numbers are similar. Whether this is a coincidence, why Sc decreases with increasing St, and how Sc changes with other disk parameters, will be investigated in the future.

Overall, there is a possible avenue to estimate the property of the suspected planet from disk observations. Since Sc is only sensitive to St in our setting (bottom panel of Figure 6),

measurements of the size and St of dust at the ring via multiwavelength dust observations and spectral energy distribution modeling (e.g., Guidi et al. 2022) or mm-wavelength polarization observations (e.g., Kataoka et al. 2016) may lead to constraints on Sc. Because the α_{turb} value and the dust ring width w_{d} may be obtained from gas and dust observations (e.g., Flaherty et al. 2020), the gas bump width w_{g} may be constrained from Equation (36) with certain assumptions on the level of ϵ_ρ. Finally, because the radial gas density profile modified by a gap-opening planet, which includes the gas bump, can be estimated analytically (e.g., Duffell 2015, 2020), the orbital radius and mass of the suspected planet may be obtained.

5. Conclusion

In this paper, we use 3D hydrodynamic simulations to study the dust kinematics in protoplanetary disks where a planet is present. Our main findings are:

1. Compared with dust rings trapped at axisymmetric pressure bumps, those trapped at planet-induced pressure bumps featuring density waves are widened by planet–disk interactions. For dust rings composed of small ($\text{St} \lesssim 10^{-2}$) grains, the fluctuations in the gas velocity field due to planetary wakes are most responsible for the widening effect.

2. Moderate dust back-reaction with local dust-to-gas ratio $\lesssim 1$ tends to narrow dust rings under the planet-related effects, compared with the cases where dust back-reaction is negligible. However, overwhelming dust back-reaction with dust-to-gas ratios of both volumetric and surface density > 1 would lead to the dust ring expanding itself while deforming the global pressure profile. In the overwhelmingly high dust mass regime, both dust back-reaction and planet-related effects are in effect, but the former takes dominance.

3. The widening effect of dust rings due to planet-related effects can be modeled by our modified gradient diffusion hypothesis, and can be quantified by a diffusion coefficient on the order of 10^{-7}–$10^{-6} R^2 \Omega_{\text{K}}$. We note that the conventional gradient diffusion hypothesis with globally constant diffusion coefficients is not applicable to our 3D disk models with planet-induced meridional flows.

4. We show that the widening effect can also be quantified by the Reynolds stress, with the corresponding turbulent viscous parameter α_{turb} on the order of 10^{-3}. However, we caution about the Schmidt number being greater than order unity. It suggests that a high momentum diffusivity of gas does not always translate to high mass diffusivity of dust, even for well-coupled dust ($\tau_{\text{s}} \ll \Omega_{\text{K}}^{-1}$) in the disk.

Appendix A
Disk Plots of Model C1 and C5

To show the differences in the gas initialization between Model C1 and C5, we plot the face-on view of gas surface density and midplane gas radial velocity in Figure 7.
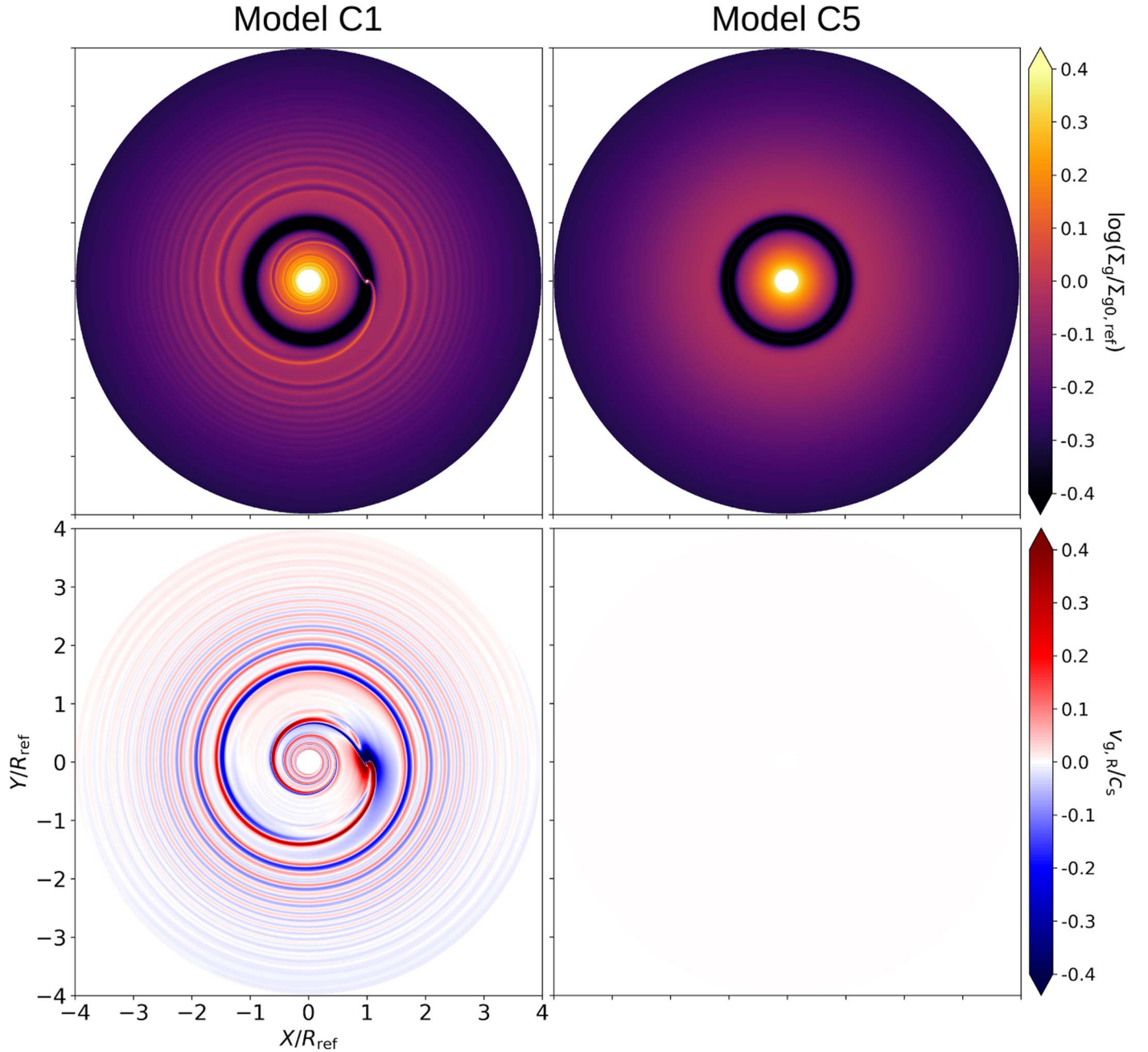

Figure 7. The gas surface density (top panels) and midplane gas radial velocity (bottom panels) of Model C1 (left panels) and C5 (right panels). Because gas evolution is stalled in type C models, all four panels are time-invariant. In Model C1, planet-related spirals in both gas density and velocity fields are preserved, whereas those in Model C5 are erased by azimuthal averaging. The bottom right panel is all white because the midplane gas in Model C5 has zero radial velocity.

Appendix B
The Mismatch between Advection and Diffusion with the Gradient Diffusion Hypothesis

Figure 8 shows the vertically integrated advection and diffusion terms from Equations (15) and (16). In the top panel, the constant diffusion tensor elements $\overline{\mathcal{D}}_R$ and $\overline{\mathcal{D}}_Z$ are identical to the ones in the top row of Figure 5. We find that the two profiles still do not match, similarly to those in Figures 5(a) and (b), even when both radial and vertical components are taken into consideration. In the bottom panel, $\overline{\mathcal{D}}_R$ and $\overline{\mathcal{D}}_Z$ are numerically fitted within the plotted range for the best match

between the two profiles. While we do not find a match as good as the ones in the middle row of Figure 5 with the modified gradient diffusion hypothesis, the fitted $\overline{\mathcal{D}}_R$ and $\overline{\mathcal{D}}_Z$ are also not realistic.

We then release the constraint of $\mathcal{D}_{ZR} = \mathcal{D}_{RZ} = 0$, allowing them to be nonzero but still constant. Figure 9 shows the fitted results in radial and vertical directions. We find the diffusion profiles still do not match the advection ones, even with the contribution from both directions considered. Therefore, a constant diffusion tensor $\overline{\mathcal{D}}$ in the original gradient diffusion hypothesis is not applicable to our models.
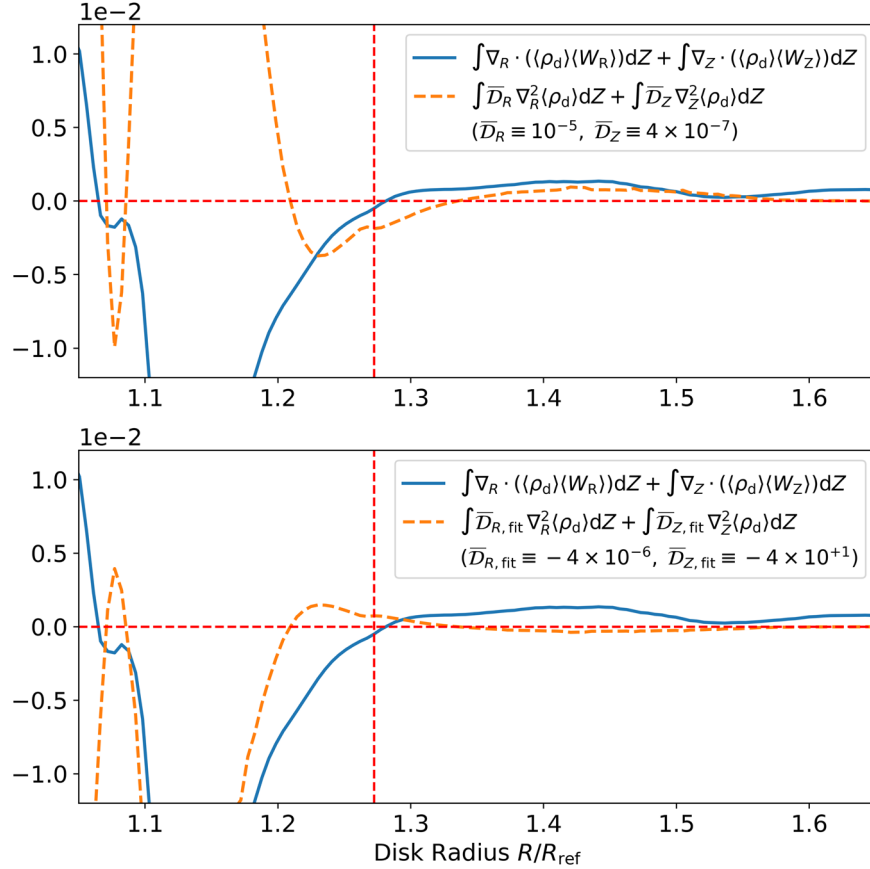

Figure 8. The radial profile of vertically integrated advection and diffusion terms with the gradient diffusion hypothesis in Section 3.3.1. All profiles are normalized to the dust surface density profile and are evaluated in the fiducial type A model at $t = 3000 T_{\rm ref}$. $\overline{\mathcal{D}}_R$ and $\overline{\mathcal{D}}_Z$ in the top panel are identical to the ones in Figures 5(a) and (b). In the bottom panel, $\overline{\mathcal{D}}_R$ and $\overline{\mathcal{D}}_Z$ are fitted within the plotted range for the best match. The unit of $\overline{\mathcal{D}}_R$ and $\overline{\mathcal{D}}_Z$ is $R_{\rm ref}^2 \Omega_{\rm K,ref}$. The horizontal red dashed line denotes $y = 0$. The vertical red dashed line denotes the dust peak at $R = 1.27 R_{\rm ref}$.
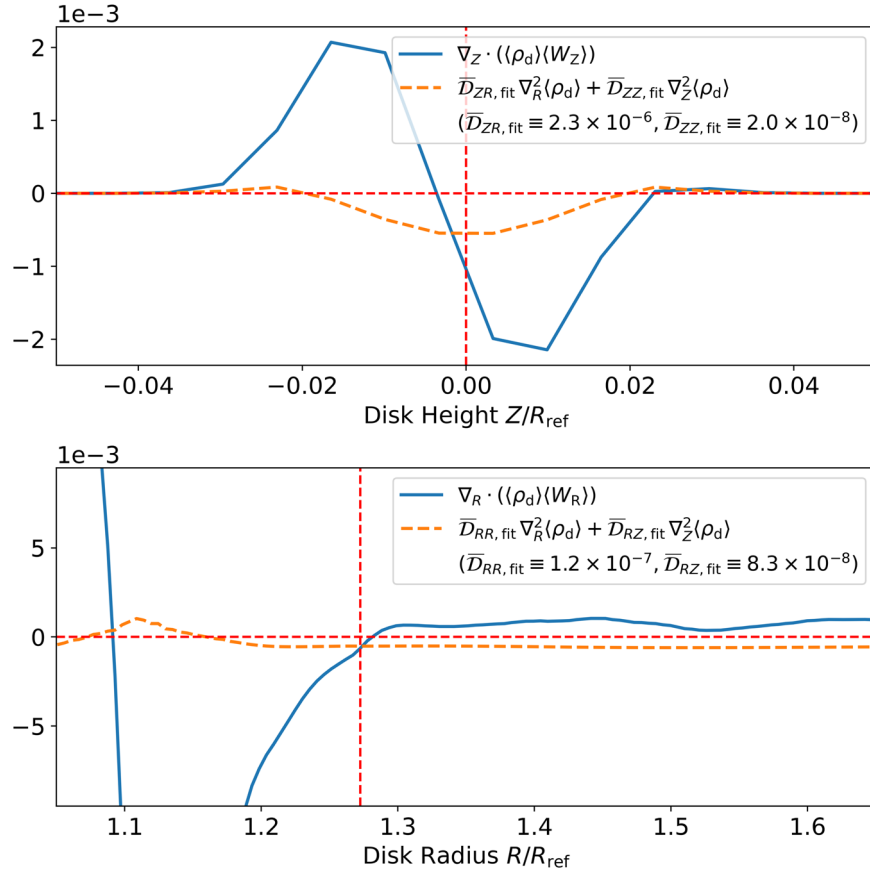
Figure 9. Similar to the panels (a) and (b) in Figure 5, but allowing $\mathcal{D}_{ZR}$ and $\mathcal{D}_{RZ}$ to be nonzero. All four diffusion coefficients are fitted within the plotted range for the best match.

Appendix C
Steps from Equations (22) to (23)

Considering Equations (20), (15), and (21), and multiplying both sides by $\langle \rho_g \rangle$, Equation (22) is written:

$$0 = \langle \rho_g \rangle \frac{\partial \langle \epsilon_\rho \rangle}{\partial t} + \langle \rho_g \rangle \langle V \rangle \nabla \langle \epsilon_\rho \rangle \tag{C1}$$

$$= \frac{\partial \langle \rho_d \rangle}{\partial t} - \langle \epsilon_\rho \rangle \frac{\partial \langle \rho_g \rangle}{\partial t} + \langle \rho_g \rangle \langle V \rangle \nabla \langle \epsilon_\rho \rangle \tag{C2}$$

$$= -\nabla \cdot (\langle \rho_d \rangle \langle W \rangle) - \nabla \cdot \langle \Delta \rho_d \Delta W \rangle + \langle \epsilon_\rho \rangle \nabla \cdot (\langle \rho_g \rangle \langle V \rangle)$$
$$+ \langle \epsilon_\rho \rangle \nabla \cdot \langle \Delta \rho_g \Delta V \rangle + \langle \rho_g \rangle \langle V \rangle \nabla \langle \epsilon_\rho \rangle \tag{C3}$$

$$= -\nabla \cdot (\langle \rho_d \rangle \langle W \rangle) - \nabla \cdot \langle \Delta \rho_d \Delta W \rangle + \nabla \cdot (\langle \epsilon_\rho \rangle \langle \rho_g \rangle \langle V \rangle)$$
$$+ \langle \epsilon_\rho \rangle \nabla \cdot \langle \Delta \rho_g \Delta V \rangle \tag{C4}$$

$$= -\nabla \cdot (\langle \rho_d \rangle \langle W - V \rangle) - \nabla \cdot \langle \Delta \rho_d \Delta W \rangle$$
$$+ \langle \epsilon_\rho \rangle \nabla \cdot \langle \Delta \rho_g \Delta V \rangle \tag{C5}$$

$$= -\nabla \cdot (\langle \rho_d \rangle \langle W - V \rangle) + \nabla \cdot (\mathcal{D} \langle \rho_g \rangle \nabla \langle \epsilon_\rho \rangle). \tag{C6}$$

ORCID iDs

Jiaqing Bi (毕嘉擎) ⑩ https://orcid.org/0000-0002-0605-4961
Min-Kai Lin (林明楷) ⑩ https://orcid.org/0000-0002-8597-4386

Ruobing Dong (董若冰) ⑩ https://orcid.org/0000-0001-9290-7846

References

ALMA Partnership, Brogan, C. L., Pérez, L. M., et al. 2015, ApJL, 808, L3
Andrews, S. M., Huang, J., Pérez, L. M., et al. 2018, ApJL, 869, L41
Benisty, M., Bae, J., Facchini, S., et al. 2021, ApJL, 916, L2
Benítez-Llambay, P., Krapp, L., & Pessah, M. E. 2019, ApJS, 241, 25
Benítez-Llambay, P., & Masset, F. S. 2016, ApJS, 223, 11
Bi, J., Lin, M.-K., & Dong, R. 2021, ApJ, 912, 107
Booth, A. S., & Ilee, J. D. 2020, MNRAS: Lett., 493, L108
Cieza, L. A., González-Ruilova, C., Hales, A. S., et al. 2021, MNRAS, 501, 2934
Currie, T., Lawson, K., Schneider, G., et al. 2022, NatAs, 6, 751
Cuzzi, J. N., Dobrovolskis, A. R., & Champney, J. M. 1993, Icar, 106, 102
Desch, S. J., Estrada, P. R., Kalyaan, A., & Cuzzi, J. N. 2017, ApJ, 840, 86
Dong, R., Liu, S.-y., Eisner, J., et al. 2018, ApJ, 860, 124
Duffell, P. C. 2015, ApJL, 807, L11
Duffell, P. C. 2020, ApJ, 889, 16
Dullemond, C. P., Birnstiel, T., Huang, J., et al. 2018, ApJL, 869, L46
Flaherty, K., Hughes, A. M., Simon, J. B., et al. 2020, ApJ, 895, 109
Fung, J., & Chiang, E. 2017, ApJ, 839, 100
Goodman, J., & Rafikov, R. R. 2001, ApJ, 552, 793
Guidi, G., Isella, A., Testi, L., et al. 2022, A&A, 664, A137
Haffert, S. Y., Bohn, A. J., de Boer, J., et al. 2019, NatAs, 3, 749
Hammer, M., Lin, M.-K., Kratter, K. M., & Pinilla, P. 2021, MNRAS, 504, 3963
Huang, J., Andrews, S. M., Cleeves, L. I., et al. 2018a, ApJ, 852, 122
Huang, J., Andrews, S. M., Dullemond, C. P., et al. 2018b, ApJL, 869, L42
Jacquet, E., Balbus, S., & Latter, H. 2011, MNRAS, 415, 3591
Jiang, H., & Ormel, C. W. 2021, MNRAS, 505, 1162
Kanagawa, K. D., Muto, T., Okuzumi, S., et al. 2018, ApJ, 868, 48
Kataoka, A., Muto, T., Momose, M., Tsukagoshi, T., & Dullemond, C. P. 2016, ApJ, 820, 54

Keppler, M., Benisty, M., Müller, A., et al. 2018, A&A, 617, A44
Koller, J., Li, H., & Lin, D. N. C. 2003, ApJL, 596, L91
Li, H., Li, S., Koller, J., et al. 2005, ApJ, 624, 1003
Li, H., Lubow, S. H., Li, S., & Lin, D. N. C. 2009, ApJL, 690, L52
Lin, D. N. C., & Papaloizou, J. C. B. 1993, ApJ, 416, 689
Lin, M.-K., & Papaloizou, J. C. B. 2010, MNRAS, 405, 1473
Long, F., Pinilla, P., Herczeg, G. J., et al. 2018, ApJ, 869, 17
Lovascio, F., & Paardekooper, S.-J. 2019, MNRAS, 488, 5290
Nelson, R. P., Gressel, O., & Umurhan, O. M. 2013, MNRAS, 435, 2610
Okuzumi, S., Momose, M., Sirono, S.-i., Kobayashi, H., & Tanaka, H. 2016, ApJ, 821, 82
Onishi, I. K., & Sekiya, M. 2017, EP&S, 69, 50
Paardekooper, S.-J., & Mellema, G. 2004, A&A, 425, L9
Portilla-Revelo, B., Kamp, I., Rab, C., et al. 2022, A&A, 658, A89

Price, D. J., & Laibe, G. 2015, MNRAS, 451, 813
Shakura, N. I., & Sunyaev, R. A. 1973, A&A, 500, 33
Takeuchi, T., & Lin, D. N. C. 2002, ApJ, 581, 1344
Taki, T., Fujimoto, M., & Ida, S. 2016, A&A, 591, A86
Tang, Y.-W., Guilloteau, S., Dutrey, A., et al. 2017, ApJ, 840, 32
Tominaga, R. T., Takahashi, S. Z., & Inutsuka, S.-i. 2019, ApJ, 881, 53
van der Marel, N., Dong, R., di Francesco, J., Williams, J. P., & Tobin, J. 2019, ApJ, 872, 112
van der Marel, N., van Dishoeck, E. F., Bruderer, S., et al. 2013, Sci, 340, 1199
Weber, P., Peréz, S., Benítez-Llambay, P., et al. 2019, ApJ, 884, 178
Youdin, A. N., & Goodman, J. 2005, ApJ, 620, 459
Youdin, A. N., & Lithwick, Y. 2007, Icar, 192, 588
Zhang, S., Zhu, Z., Huang, J., et al. 2018, ApJL, 869, L47